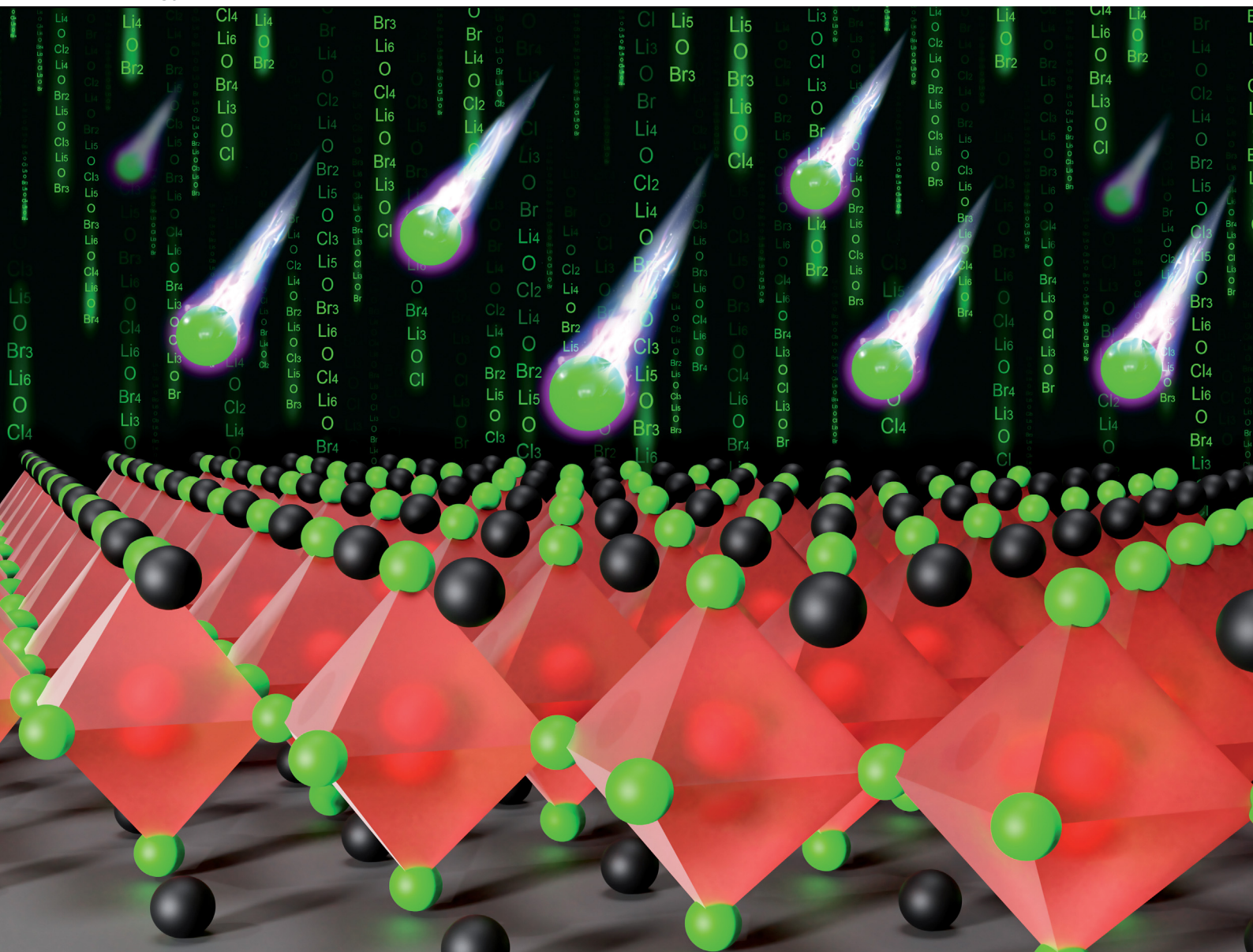


# Energy Advances

Volume 2  
Number 5  
May 2023  
Pages 567–740

[rsc.li/energy-advances](https://rsc.li/energy-advances)



ISSN 2753-1457

**PAPER**

James A. Dawson *et al.*  
Defect chemistry and ion transport in low-dimensional-  
networked Li-rich anti-perovskites as solid electrolytes  
for solid-state batteries

Cite this: *Energy Adv.*, 2023,  
2, 653

# Defect chemistry and ion transport in low-dimensional-networked Li-rich anti-perovskites as solid electrolytes for solid-state batteries†

Ana Carolina Coutinho Dutra,<sup>id</sup><sup>a</sup> George E. Rudman,<sup>id</sup><sup>ab</sup> Karen E. Johnston<sup>id</sup><sup>b</sup>  
and James A. Dawson<sup>id</sup><sup>\*ac</sup>

Solid-state batteries are attracting significant attention due to their plethora of potential advantages, including energy density gains and safety enhancements. The heart of this technology can be found in its solid electrolytes and thus its progress is intrinsically attached to the discovery and understanding of novel solid electrolyte materials. In recent years, Li-rich anti-perovskites have become promising solid electrolyte candidates as they combine high ionic conductivity, structural versatility and stability against Li metal. Here, the energetics of defect formation, stability, Li-ion transport and fluorine doping in a range of  $\text{Li}_x\text{OX}_{x-2}$  ( $X = \text{Cl}$  or  $\text{Br}$ ;  $x = 3-6$ ) anti-perovskites with zero- to three-dimensional-networked structures are explored *via* atomistic simulations. Our calculations show that these materials generally present Li-halide Schottky defect pairs as the dominant native defects. We find that defect formation is generally energetically more favourable in the  $\text{Li}_x\text{OCl}_{x-2}$  series compared to the equivalent structures in the  $\text{Li}_x\text{OBr}_{x-2}$  set. Additionally, our molecular dynamics simulations reveal the strong relationship between Li-ion dynamics and dimensionality in these materials, namely, increasing Li-ion diffusion and decreasing activation energy with reduced dimensionality. Enhanced Li-ion diffusion is observed for the low-dimensional-networked Br-based materials ( $4.81 \times 10^{-9}$  and  $6.08 \times 10^{-9}$   $\text{cm}^2 \text{s}^{-1}$  for  $\text{Li}_5\text{OBr}_3$  and  $\text{Li}_6\text{OBr}_4$  at 300 K, respectively) compared to their Cl-based counterparts ( $9.85 \times 10^{-10}$  and  $2.06 \times 10^{-9}$   $\text{cm}^2 \text{s}^{-1}$  for  $\text{Li}_5\text{OCl}_3$  and  $\text{Li}_6\text{OCl}_4$  at 300 K, respectively), illustrating the importance of lattice polarizability in these soft and unstable materials. This is further exemplified by the significant reduction in Li-ion diffusion and increase in activation energies observed in F-doped  $\text{Li}_x\text{OX}_{x-2}$ .

Received 16th February 2023,  
Accepted 18th March 2023

DOI: 10.1039/d3ya00075c

rsc.li/energy-advances

## 1. Introduction

Advances in energy storage technologies are fundamental for achieving net-zero emissions as they drive the electrification of transport and the efficient large-scale storage of intermittently generated renewable energy. Current Li-ion batteries, however, are not capable of meeting the performance, safety and cost requirements that future energy storage devices will impose and solely refining existing technologies in an incremental manner will not be sufficient to power future leading-edge applications.<sup>1-5</sup>

Solid-state batteries represent a next-generation technology currently attracting significant interest due to their potential to

revolutionise energy storage. Solid-state batteries display an abundance of potential advantages when compared to liquid electrolyte architectures, including reduced costs and improved energy density, voltage, cycle life and safety profiles.<sup>5-10</sup> Despite their promising nature, their widespread utilisation is still significantly blocked by various challenges, including lithium dendrite growth, low ionic conductivity, electrochemical stability, interfacial resistance and large-scale solid electrolyte synthesis.<sup>5,9-12</sup> Given the central role that solid electrolytes possess in solid-state batteries, the continuous pursuit of understanding and designing novel solid electrolyte materials is vital for the future of this field.

Li-rich anti-perovskites have the typical formula of  $\text{Li}_3\text{OX}$  ( $X = \text{Cl}$ ,  $\text{Br}$ ,  $\text{I}$  or a mixture of halides) and are capturing significant interest as a solid electrolyte family endowed with promising features, including good Li-ion conductivity, stability against Li metal, wide electrochemical windows and low-cost synthesis.<sup>13-17</sup> Anti-perovskites also benefit from a remarkably versatile structure that allows for easy structural manipulation, enabling the tailoring of performance, properties and ion

<sup>a</sup> Chemistry – School of Natural and Environmental Sciences, Newcastle University, Newcastle upon Tyne, NE1 7RU, UK. E-mail: james.dawson@newcastle.ac.uk

<sup>b</sup> Department of Chemistry, Durham University, Durham, DH1 3LE, UK

<sup>c</sup> Centre for Energy, Newcastle University, Newcastle upon Tyne, NE1 7RU, UK

† Electronic supplementary information (ESI) available. See DOI: <https://doi.org/10.1039/d3ya00075c>



transport mechanisms, as well as providing substantial chemical versatility and diversity.<sup>18–22</sup>

The accurate measurement of the Li-ion conductivities and activation energies in anti-perovskite solid electrolytes has gained fresh prominence in the context of recent findings. While an early study by Zhao and Daemen<sup>13</sup> on Li<sub>3</sub>OCl, Li<sub>3</sub>OBr and Li<sub>3</sub>OCl<sub>0.5</sub>Br<sub>0.5</sub> reported Li-ion conductivities of  $>10^{-3}$  S cm<sup>-1</sup> at room temperature and activation energies of 0.2–0.3 eV, more recent works have obtained activation energies of  $\sim 0.6$  eV and lower conductivities (e.g.,  $10^{-6}$  S cm<sup>-1</sup> at room temperature) for bulk Li<sub>3</sub>OCl and Li<sub>3</sub>OBr.<sup>14,19,23–30</sup> Several reasons for this disparity, including high grain boundary resistance, unintended doping and the presence of moisture (e.g., Li<sub>2</sub>OHCl), have been proposed.<sup>14,18,23,24,26,27,29,31–37</sup>

Such discrepancies have highlighted the importance of atomistic modelling studies in accessing fundamental information on the ion transport mechanisms and defect chemistry present in Li-rich anti-perovskites,<sup>22–25,29–31,38–50</sup> contributing to unravelling the underlying processes that cause their intriguing behaviour. In particular, significant efforts have been made to determine the dominant defect types in anti-perovskites and how they affect their ionic diffusion.<sup>21,43,44,48,51</sup> For example, in a density functional theory (DFT) study of Li<sub>3</sub>OCl, Li<sub>3</sub>OBr and Li<sub>3</sub>OCl<sub>0.5</sub>Br<sub>0.5</sub>, Emly *et al.*<sup>43</sup> investigated a three-ion hop mechanism that involved Li interstitial dumbbells that promoted a very low Li-ion migration barrier of  $\sim 0.17$  eV for all systems, indicating a concerted Li-ion motion that is seen in several other solid electrolytes.<sup>28,49–56</sup> However, the high formation energies of Li interstitials found for these structures suggested that this mechanism was not responsible for the high conductivities found. Mouta *et al.*<sup>44</sup> also found a low enthalpy of 0.13 eV for interstitial migration in Li<sub>3</sub>OCl *via* classical atomistic quasi-static calculations. However, their explorations deemed vacancy migration, with a vacancy migration enthalpy of 0.30 eV, to be the pertinent transport mechanism in the system due to the

concentration of Li vacancies being six orders of magnitude greater than the one found for Li interstitials. The dominance of vacancy hopping mechanisms from interstitial diffusion was also reported by Dawson *et al.*<sup>23</sup> in a study that explored the defect chemistry of a wide range of Li<sub>3–x</sub>Na<sub>x</sub>OCl<sub>1–y</sub>Br<sub>y</sub> anti-perovskites.

In addition to the well-reported three-dimensional-networked (3DN) anti-perovskites discussed above, low-DN Cl-based anti-perovskites (*i.e.*, 2DN Li<sub>4</sub>OCl<sub>2</sub>, 1DN Li<sub>5</sub>OCl<sub>3</sub> and 0DN Li<sub>6</sub>OCl<sub>4</sub>) have recently been considered by Lu *et al.*<sup>57</sup> based on advances in low-DN hybrid perovskites for photovoltaic applications.<sup>58</sup> Using DFT and *ab initio* molecular dynamics (AIMD) simulations, the authors found that the Li-ion conductivity increases with decreasing dimensionality due to the decreased ion migration bottlenecks and the softening of the rotation modes of the OLi<sub>6</sub> octahedra. The structures of these materials are presented in Fig. 1.

Although the synthesis of such 1DN and 0DN anti-perovskites has yet to be reported, recent progress in terms of synthesising 2DN Br-based anti-perovskites has been made. Zhu *et al.*<sup>59</sup> were successful in synthesising a mixture of 2DN Li<sub>7</sub>O<sub>2</sub>Br<sub>3</sub> and 3DN Li<sub>3</sub>OBr anti-perovskites, which possessed enhanced ionic conductivity ( $5 \times 10^{-5}$  S cm<sup>-1</sup>) compared to Li<sub>3</sub>OBr alone ( $10^{-6}$  S cm<sup>-1</sup>), suggesting the possibility of low-DN anti-perovskites displaying higher ionic conductivities than their 3DN counterparts. Wakazaki *et al.*<sup>60</sup> recently synthesised Li<sub>4</sub>OBr<sub>2</sub>, a member of the inverse Ruddlesden–Popper family, for the first time by high-pressure synthesis. The authors experimentally measured the activation energy of Li-ion conduction in this system as 0.63 eV and this was further lowered by halide (F and I) substitution and the addition of Li–Br defects. Advances have also been made for the synthesis of 2DN Na-based low-DN anti-perovskites, with Zhu *et al.*<sup>41</sup> reporting the synthesis of Na<sub>4</sub>OI<sub>2</sub> (first reported by Sabrowsky *et al.*<sup>61</sup>) *via* a solid-state reaction.

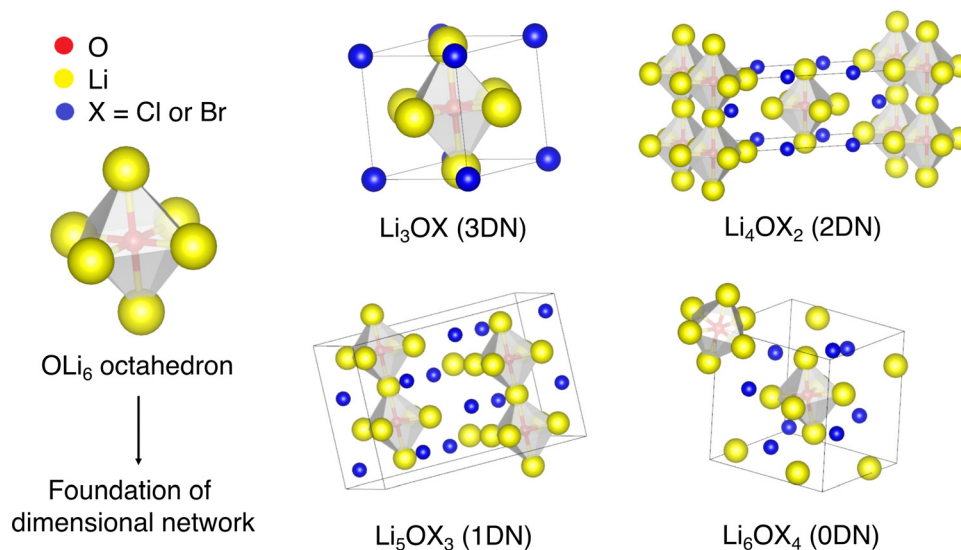


Fig. 1 Schematic representation of OLi<sub>6</sub> octahedron as the foundation of the cation network and crystal structures of Li<sub>x</sub>OX<sub>x–2</sub> (X = Cl or Br; x = 3–6) anti-perovskites.



Despite the considerable body of work focused on anti-perovskites, many of the elementary processes that explain their behaviour are still misunderstood. For low-DN anti-perovskites, the ion transport mechanisms and defect chemistry are yet to be fully explored and understood. Considering the pivotal role that ionic diffusion and structural disorder have on the ion transport behaviour of anti-perovskites, there is a heightened need for studies that investigate these factors in these materials.

In this study, we use classical defect simulations to investigate the energetics of defect formation in the composition range of  $\text{Li}_x\text{OX}_{x-2}$  ( $X = \text{Cl}$  or  $\text{Br}$ ;  $x = 3-6$ ) anti-perovskites with 3DN to 0DN structures. Additionally, large-scale molecular dynamics (MD) studies for a range of temperatures (200–800 K) are carried to calculate the Li-ion diffusion activation energy of these systems. Our results reveal the strong relationship between defect chemistry, stability, Li-ion dynamics and dimensionality in these materials, namely, increasing Li-ion diffusion and decreasing activation energy and defects formation energy with reduced dimensionality. Our simulations also show the impact different halides have on defect formation, with lower formation energies found for Cl-containing systems. Finally, we also consider the role of fluorine doping in these materials as a potential method of improving their Li-ion conductivity but find that it actually significantly reduces the Li-ion conductivity and increases the activation energy. The results reported here strengthen our current understanding of the chemistry of low-DN anti-perovskites, contributing to the guidance of future experimental decisions and comprehending their potential as solid electrolytes in the urgent quest of finding novel materials that could make energy storage safer, more efficient and, most importantly, more sustainable.

## 2. Methodology

The procedures followed to perform both the defect and classical MD calculations in this work are based on well-established protocols that have been widely and successfully used to explore defect energetics and ion transport mechanisms in a wide range of battery materials.<sup>62–67</sup>

### 2.1 Structural details

The structural details (*e.g.*, lattice parameters and atomic sites) for the  $\text{Li}_3\text{OCl}$  system were obtained from the Materials Project repository,<sup>68</sup> while the details for the remaining investigated anti-perovskites were taken from the work by Lu *et al.*<sup>57</sup> The structural details for  $\text{Li}_2\text{O}$ ,  $\text{LiCl}$  and  $\text{LiBr}$  were also needed for the purpose of calculating the partial Schottky defect formation energies and were also obtained from the Materials Project repository. The optimised structures and lattice parameters of all explored 3DN, 2DN, 1DN and 0DN anti-perovskites are attached as CIFs in the ESI.†

### 2.2 Potential model

The Buckingham potential model of Mouta *et al.*,<sup>44</sup> with refinements from Dawson *et al.*,<sup>23</sup> was used herein for all the calculations. This model has previously been used to

successfully describe Li-rich anti-perovskites for the exploration of their defect chemistry and ion transport behaviour. The fluorine interactions were taken from Clarke *et al.*<sup>28</sup> The long-range ionic interactions were modelled using Coulombic terms. Formal valence charges were used for all ions. The shell model of Dick and Overhauser<sup>69</sup> was used to account for ionic polarisation. This model divides each ion into a core, which is constituted of the nucleus and inner electrons, and a massless shell, which is formed solely by the valence electrons. The core and shell are connected by a harmonic spring of constant  $k$ .

### 2.3 Defect formation energy calculations

A wide range of defect types (including full Schottky, alkali-halide partial Schottky,  $\text{Li}_2\text{O}$  partial Schottky, antisite and lithium, oxygen and halide Frenkel defects) and fluorine doping were investigated in the selected anti-perovskites using the General Utility Lattice Program (GULP)<sup>70</sup> with the Mott–Littleton approximation.<sup>71</sup> The creation of a defect significantly impacts the atoms surrounding the defect centre as it generates a Coulombic perturbation in the disordered region. Therefore, to account for the lattice relaxation around the defect centre, the Mott–Littleton approximation divides the area around the created defect into two spherical regions. The first region, region I, is closest to the defect centre and includes the defect centre itself and all ions surrounding it. Due to the proximity of region I to the defect centre and thus to the origin of perturbation, the lattice relaxation in this region will be stronger than in any other regions and the relaxation of the ions will be calculated explicitly for region I. The second region, region II, starts at the border of region I and extends to infinity. This region is subdivided into region IIa, closest to the defect centre, and region IIb. The relaxation of ions in region IIa is allowed and is considered as impacted by the central defect, whereas region IIb is treated as continuous and the impact of the defect is considered to only be dielectric. For our calculations, we used radii of 13 and 21 Å for regions I and IIa, respectively.

### 2.4 Molecular dynamics calculations

The LAMMPS code<sup>72</sup> was used to perform all MD simulations. An example LAMMPS input file is given in the ESI.† Long MD runs of 10 ns were completed using a time step of 2 fs with supercells of  $10 \times 10 \times 10$ . Long-range Li-ion diffusion was achieved by randomly removing  $\sim 2\%$  of Li and halide ions from the structures. The constant-temperature, constant-pressure ensemble (*NPT*) was used in all simulations with a Nosé–Hoover thermostat.<sup>73</sup> The MD simulations were run for a temperature range of 500–800 K at intervals of 100 K for all systems and for an additional temperature range of 200–400 K at intervals of 50 K for the 1DN and 0DN systems. Self-diffusion data for the Li ions were acquired from the mean-squared displacement (MSDs) according to:

$$\langle r_i^2(t) \rangle = 6D_{\text{Li}}t \quad (1)$$

where  $\langle r_i^2(t) \rangle$  is the MSD,  $D_{\text{Li}}$  is the diffusion coefficient for Li ions and  $t$  is time.



### 3. Results and discussion

#### 3.1 Structures, stability and intrinsic defect formation

In the  $ABX_3$  perovskite structure, cations occupy the A and B sites while the X site is populated by an anion. Alternatively, in anti-perovskites, the A and B sites are occupied by anions while a cation occupies the X site. As illustrated for  $Li_3OX$  ( $X = Cl$  or  $Br$ ) in Fig. 1, in the anti-perovskite structure, the  $O^{2-}$  anion at the B site is octahedrally coordinated to six X-site  $Li^+$  cations and the A-site halide anions are cuboctahedrally coordinated to twelve nearest-neighbour cations.<sup>17</sup>

Structurally, in an  $ABX_3$  anti-perovskite (space group  $Pm\bar{3}m$ ), a 3D network for the cation is formed as the cations on the vertices are shared by neighbouring  $BX_6$  sets, establishing octahedra that will form a cubic (sub)lattice that represents the foundation of the cation 3D network.<sup>57</sup> The connectivity between these octahedra enables the hopping of the cations, which is a process that has been linked to the high ionic conductivities that anti-perovskites display.

Lu *et al.*<sup>57</sup> recently introduced the concept of low-dimensional-networked (low-DN) anti-perovskites, which are formed when the dimensionality of the interconnected  $BX_6$  octahedra is lowered. In the 2DN anti-perovskite (space group  $I4/mmm$ ), the  $BX_6$  octahedra are connected along planes separated by  $LiX$  ( $X = Cl$  or  $Br$ ) layers. Analogously, if a 2DN anti-perovskite is further sliced perpendicular to the inorganic sheets, the octahedra remain connected only along one axis, thereby forming a 1DN anti-perovskite (space group  $Pnam$ ). 0DN (space group  $R\bar{3}c$ ) anti-perovskites are derived by the further slicing of a 1DN anti-perovskite to form nonconnected (*i.e.*, isolated) octahedra. Additional details regarding the nomenclature and structures of low-DN perovskites are available in the review of Saidaminov *et al.*<sup>58</sup>

To assess the stability of these materials, we calculated their formation energies with respect to their starting oxides (*i.e.*,  $Li_2O$  and  $LiX$  ( $X = Cl$  or  $Br$ )). For the Cl-based materials, we obtained values of  $-0.60$ ,  $-0.63$ ,  $-0.44$  and  $-0.08$  eV for the 3DN, 2DN, 1DN and 0DN systems, respectively. These energies are in good agreement with the decomposition energies calculated by Lu *et al.*<sup>57</sup> using DFT for the same systems, *i.e.*, 2DN  $Li_4OCl_2$  is predicted to be the most thermodynamically stable and 0DN  $Li_6OCl_4$  Li is predicted to be the least thermodynamically stable at 0 K. For the Br-based materials, we obtained values of  $-0.93$ ,  $-1.06$ ,  $-0.85$  and  $-0.64$  eV for the 3DN, 2DN, 1DN and 0DN systems, respectively. Our calculations therefore suggest that the Br-based materials are more stable than their Cl-based counterparts. A similar finding was also reported by Lu *et al.*<sup>57</sup> for the 3DN and 0DN materials. These results highlight the clear reduction in stability with reducing dimensionality in these materials.

Different types of intrinsic defects have different characteristics, which can cause them to impact ion transport and conductivity within a material differently. Therefore, the investigation of intrinsic defect energetics can provide a wealth of information, not only regarding the defect chemistry of a system but also its ion transport mechanisms.

Herein, we computed the energetics of intrinsic Schottky, Frenkel and antisite defects in a wide range of  $Li_xOX_{x-2}$  ( $X = Cl$  or  $Br$ ;  $x = 3-6$ ) anti-perovskites with 3DN to 0DN structures. All the defect types explored in this study are given below in Kröger-Vink notation for the Cl-based materials (equivalent equations for the Br-based materials can be formulated by simply replacing Cl with Br):

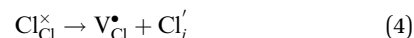
Li Frenkel:



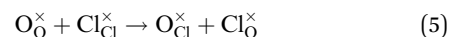
O Frenkel:



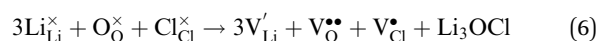
Cl Frenkel:



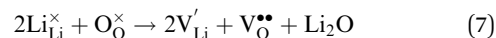
Antisite:



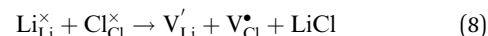
Full Schottky:



$Li_2O$  partial Schottky:



Li-halide partial Schottky:



The calculated formation energies for these intrinsic defects in the investigated systems are presented in Fig. 2. These energies are for the lowest energy (most stable) defect configurations obtained in each system. Given that a lower defect formation energy indicates its more energetically favourable formation, the results in Fig. 2 reveal key information related to the concentration of intrinsic defects in the analysed materials and therefore their potential role in Li-ion diffusion.

First, the results show that the formation of almost all defects in both the Cl- and Br-based materials explored becomes energetically more favourable when the dimensions are reduced for the 3DN to 0DN materials, with the only exception being the full Schottky defect pairs. This trend is in accordance with previous literature findings for the Cl-based materials.<sup>57</sup> The calculations also suggest that the formation of the great majority of defect types is more energetically favourable in Cl-based structures if compared to their equivalent Br-containing systems. This relationship found between defect formation energy and the nature of the halide contained in a system is in agreement with previous simulations results reported for  $Li_3OCl$ ,  $Li_2NaOCl$  and  $LiNa_2OCl$  and their Br-containing counterparts.<sup>23</sup> This potential for higher defect concentrations in their structures suggest that systems with lower dimensions and with Cl instead of Br as their chosen halide can potentially present enhanced Li-ion transport and conductivity, albeit with a concomitant reduction in stability.



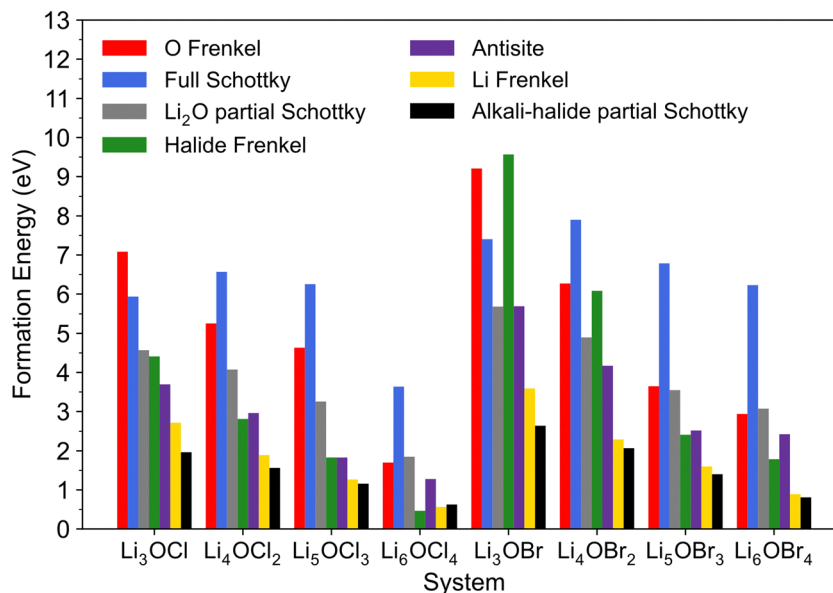


Fig. 2 Calculated formation energies for Schottky, Frenkel and antisite defects in  $\text{Li}_x\text{OX}_{x-2}$  ( $X = \text{Cl}$  or  $\text{Br}$ ;  $x = 3-6$ ) anti-perovskites.

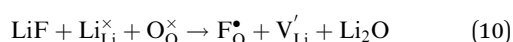
The comparison of the results across the different halide sets also shows that the concentrations of halide Frenkel defects in the 3DN and 2DN Br-containing structures are expected to be significantly lower than those for their counterparts in the Cl set based on the calculated formation energies. Additionally, whereas almost all these systems are predicted to present Li-halide Schottky defect pairs as dominant native defects, which aligns with previous literature reports for  $\text{Li}_3\text{OCl}$ ,<sup>23</sup> Cl interstitials are the predicted dominant type of intrinsic disorder in  $\text{Li}_6\text{OCl}_4$ . This result suggests that  $\text{Li}_6\text{OCl}_4$  may present interstitial diffusion as the main ion transport mechanism and not a Li vacancy hopping mechanism, in contrast to the other anti-perovskites investigated, as well as to what has been predicted for this structure in the literature previously.<sup>57</sup> Frenkel-type defects have been reported to be more mobile in anti-perovskites and other important solid electrolytes and present lower migration barriers than other types of defects,<sup>43,44,55,74</sup> which could potentially lead to more favourable ion transport mechanisms in systems possessing higher concentrations of Frenkel-type defects. Therefore, these results indicate that Li-ion transport and conductivity could be enhanced in  $\text{Li}_6\text{OCl}_4$  compared to the other investigated systems, as also discussed below.

In addition to the intrinsic defects discussed above, we also considered the energetics of doping fluorine into these anti-perovskites as a potential route to increasing their Li-ion conductivity.  $\text{F}^-$  dopant ions can occupy either the halide or oxygen site in anti-perovskites, as illustrated for the Cl-based materials below:

F doping at Cl site:



F doping at O site:



The two possible doping site raises the question of which is more energetically favourable and therefore more likely to be occupied.

Fig. 3 shows the calculated energies for the F doping of  $\text{Li}_x\text{OX}_{x-2}$  ( $X = \text{Cl}$  or  $\text{Br}$ ;  $x = 3-6$ ) considering both occupation at the halide and oxygen sites. The results indicate that the energies are significantly higher for fluorine doping on the oxygen site, suggesting that the isovalent fluorine doping mechanism (eqn (1)) is the energetically favourable doping mechanism in these systems. This finding was also previously reported for  $\text{Li}_3\text{OCl}$ .<sup>28</sup> Furthermore, we can see that the 2DN materials have the highest energies associated with fluorine doping on the halide site. For the Cl-based materials, the 0DN configuration provides the lowest energy and hence the most favourable structural motif for fluorine doping. In contrast, for the Br-based systems, the 1DN material provides the most preferential environment for fluorine incorporation.

It is well known that point defects can interact with one another, especially when they are oppositely charged, to form localised defect clusters that can influence ion transport. Clarke *et al.*<sup>28</sup> recently suggested that high binding energies between  $\text{F}^-$  doped on the O site and  $\text{V}_{\text{Li}}'$  in  $\text{Li}_3\text{OCl}$  likely arise due to the small Li–O interatomic spacing ( $< 2 \text{ \AA}$ ). The clustering of  $\text{F}^-$  ions and  $\text{V}_{\text{Li}}'$  throughout the structure was found to inhibit long-range Li-ion migration. On this basis, we calculated the binding energies (Fig. 4) that arise from the interaction between oppositely charged  $\text{F}_{\text{O}}^{\bullet}$  and  $\text{V}_{\text{Li}}'$  through the aliovalent fluorine doping mechanism (eqn (10)). These energies give insight into potential  $\text{F}_{\text{O}}^{\bullet} - \text{V}_{\text{Li}}'$  pair formation and therefore long-range Li-ion mobility. Our results show that F doping on the oxygen site results in high binding energies of greater than  $-0.5 \text{ eV}$  in all systems modelled except for  $\text{Li}_5\text{OCl}_3$ . The magnitude of these binding energies will also substantially



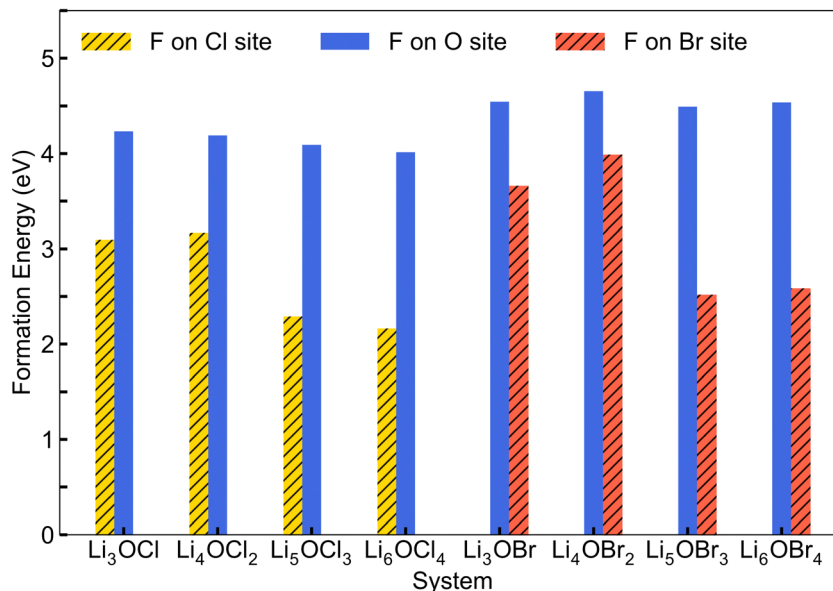


Fig. 3 Calculated formation energies for fluorine doping of  $\text{Li}_x\text{OX}_{x-2}$  ( $X = \text{Cl}$  or  $\text{Br}$ ;  $x = 3-6$ ) anti-perovskites.

reduce the energy required for F doping at the oxygen site. In fact, if we were to combine the formation energies in Fig. 3 for F doping at the oxygen site with the binding energies in Fig. 4, the overall energies for F doping at the halide or oxygen site become similar. This suggests the possibility of F doping at both sites depending on the synthesis conditions employed.

Given the critical role that Li vacancies have in determining the Li-ion conductivity of these materials, such binding energies represent a significant potential hindrance to their performance as solid electrolytes. Furthermore, the binding energies calculated for the Br-based systems are significantly higher than those calculated for the equivalent Cl-based systems. Therefore, these results suggest that F doping in these

anti-perovskites may have a detrimental effect on their Li-ion conducting properties but this must be confirmed using MD simulations.

### 3.2 Li-ion transport

To investigate Li-ion diffusion in these anti-perovskite systems, we conducted MD calculations for all the selected materials with a representative Li-halide Schottky defect concentration of  $\sim 2\%$ . Li-halide Schottky defect pairs were the defect type chosen for the MD calculations as these have been confirmed as the dominant disorder for all systems analysed except for  $\text{Li}_6\text{OCl}_4$ , as discussed above.

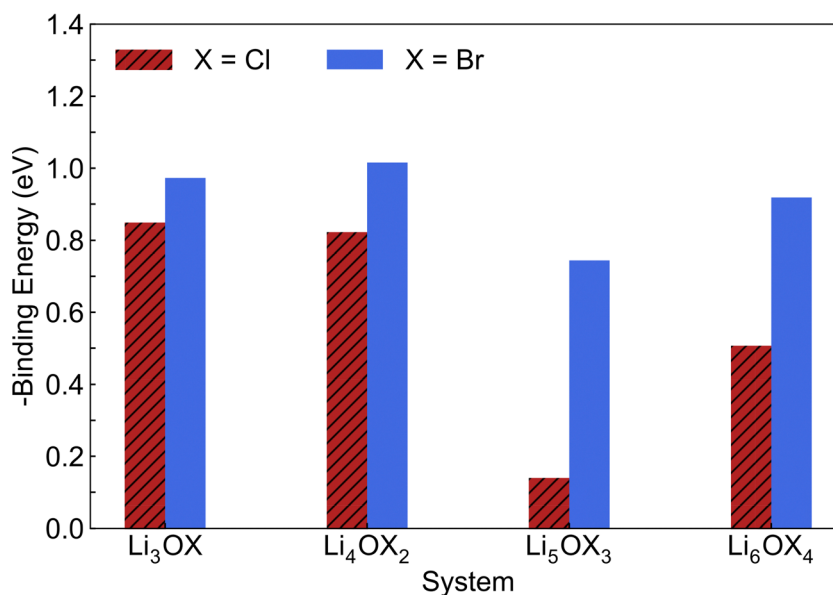


Fig. 4 Calculated binding energies for fluorine doping of  $\text{Li}_x\text{OX}_{x-2}$  ( $X = \text{Cl}$  or  $\text{Br}$ ;  $x = 3-6$ ) anti-perovskites at the oxygen site.



The self-diffusion coefficients obtained *via* MSD plots as a function of time along with their corresponding temperatures were used to produce the Arrhenius plots in Fig. 5, which were used to calculate the activation energies for Li-ion conductivity for all systems. Example MSD plots for the Br-based structures at a representative temperature of 700 K are given in Fig. S1 (ESI<sup>†</sup>).

The Arrhenius plots in Fig. 5 reveal that the low-dimensional-networked systems (1DN and 0DN) exhibit a strong increase in Li-ion diffusion above  $\sim 300$  K, which prevents the data across the whole temperature range for these materials to be described by a single linear fit. To determine the reason for such a significant increase in Li-ion diffusion at relatively modest temperatures for these low-dimensional-networked systems, we computed all their possible radial distribution functions (RDFs) throughout the MD simulations, as shown in Fig. S2 (ESI<sup>†</sup>) for 300 K.

There is a clear distinction between the structures of the 3DN ( $\text{Li}_3\text{OX}$ ) and 2DN ( $\text{Li}_4\text{OX}_2$ ) structures compared to the 1DN

( $\text{Li}_5\text{OX}_3$ ) and 0DN ( $\text{Li}_6\text{OX}_4$ ) systems. While the high-dimensional-networked systems show distinct peaks for all elemental combinations across the entire range of interatomic distances ( $r$ ), the low-dimensional-networked systems present remarkably flat RDFs at  $>5$  Å, indicative of a solid-to-liquid transition, *i.e.*, melting. This discrepancy is further verified by the smooth curves for the integrated RDFs of the 1DN and 0DN materials, which indicate an almost linear increase in coordination number with increasing  $r$ . In contrast, for the 3DN and 2DN anti-perovskites, regular plateaus are observed where the coordination number remains unchanged with increasing  $r$ , thereby highlighted their highly ordered crystalline structures. The effect of temperature on the RDFs in these materials is illustrated in Fig. 6 for the example of Li–Li at 300 and 600 K. These plots again show the increase in disorder with decreasing dimensionality in the systems. At 600 K, this trend becomes even clearer with the Li–Li RDFs for the 1DN and 0DN material presenting liquid-like behaviour beyond 3 Å.

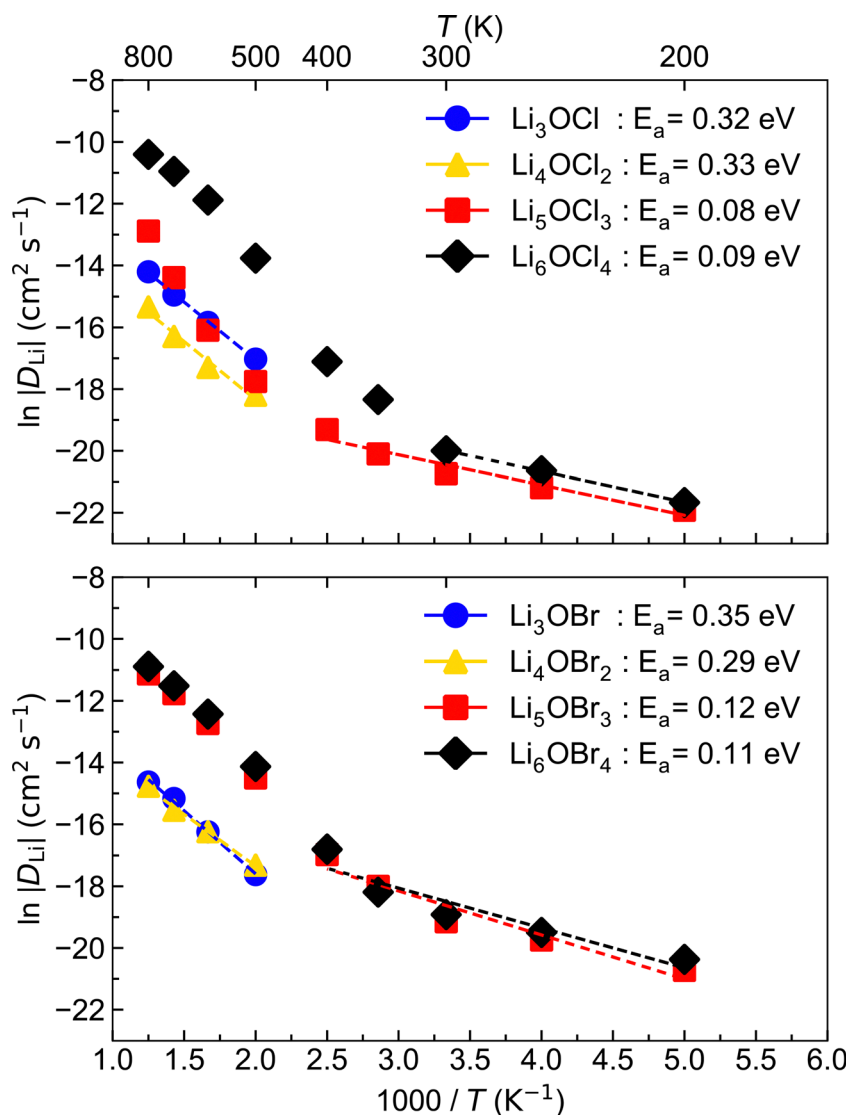


Fig. 5 Arrhenius plots of Li-ion diffusion for  $\text{Li}_x\text{OX}_{x-2}$  ( $X = \text{Cl}$  or  $\text{Br}$ ;  $x = 3-6$ ) anti-perovskites.





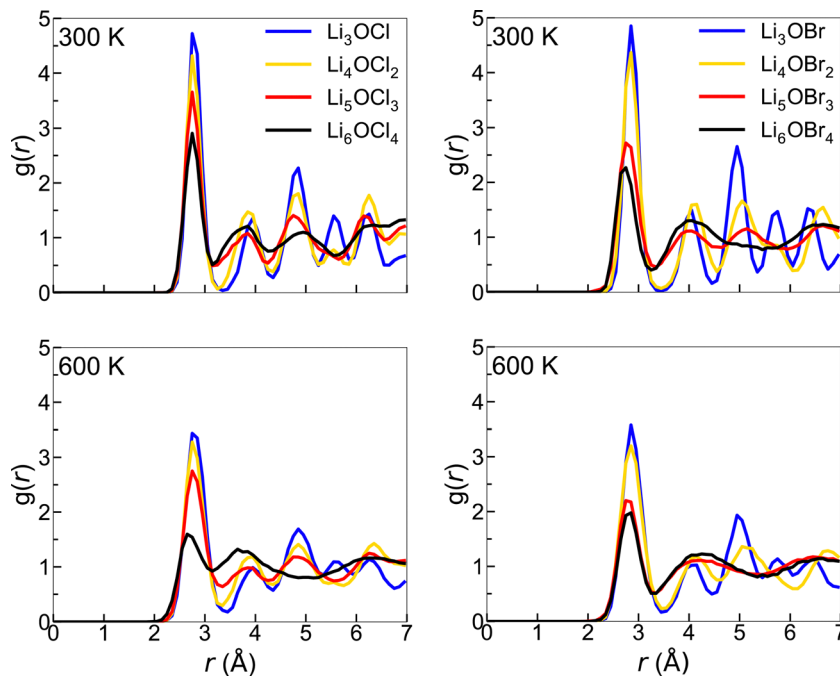


Fig. 6 Li-Li RDFs for  $\text{Li}_x\text{OX}_{x-2}$  ( $X = \text{Cl}$  (left) or  $\text{Br}$  (right);  $x = 3-6$ ) anti-perovskites at 300 and 600 K.

Although Lu *et al.*<sup>57</sup> reported the melting of  $\text{Li}_5\text{OCl}_3$  at 800 K in their smaller scale DFT simulations, this is the first time the melting of these 1DN and 0DN anti-perovskites at temperatures as low as 300 K has been reported. This melting at low temperatures is indicative of instability (and therefore super-ionic Li-ion conductivity) in the 1DN and 0DN systems, which is reasonable considering the low dimensionality within the structures and the fact that the feasibility of their synthesis is still yet to be confirmed experimentally.

The comparison of the self-diffusion coefficients obtained at 300 K for all systems in Fig. 7 reveals the clear relationship

between Li-ion dynamics and dimensionality in these materials, with Li-ion diffusion increasing and the associated activation energy decreasing with reducing dimensionality. The calculated values and observed trends are in excellent agreement with the DFT results of Lu *et al.*<sup>57</sup> for the Cl-based materials, who ascribed their findings to the enlarged bottleneck sizes for Li-ion hopping and the softening of the lattice with reducing dimensionality. The calculated activation energies for  $\text{Li}_3\text{OCl}$  (0.32 eV) and  $\text{Li}_3\text{OBr}$  (0.35 eV) are also similar to those predicted by Dawson *et al.*<sup>23</sup> (0.29 and 0.31 eV, respectively). It is noteworthy that these calculated values are significantly lower than recently reported

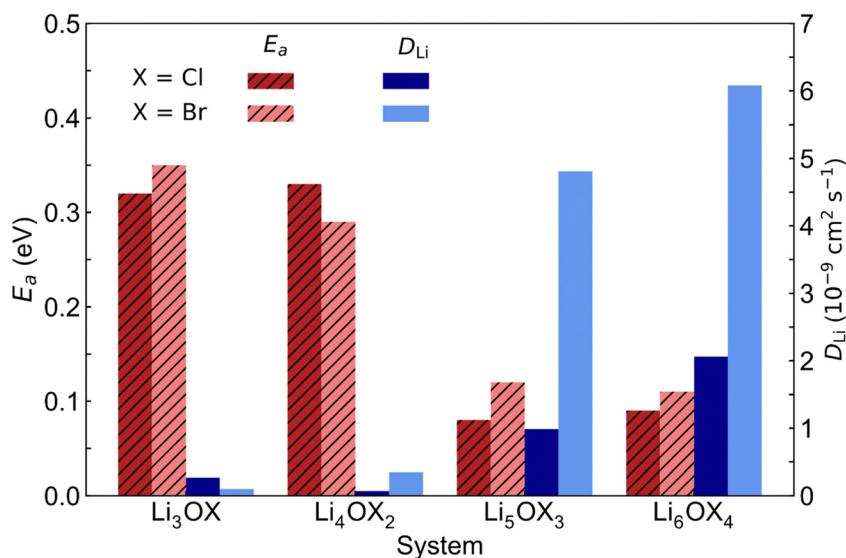


Fig. 7 Self-diffusion coefficients ( $D_{\text{Li}}$ ) at 300 K and activation energies ( $E_a$ ) for Li-ion diffusion in  $\text{Li}_x\text{OX}_{x-2}$  ( $X = \text{Cl}$  or  $\text{Br}$ ;  $x = 3-6$ ) anti-perovskites.



experimental results ( $\sim 0.6$  eV),<sup>17</sup> which has been ascribed to the high grain boundary resistance in these materials that is not typically accounted for in atomistic simulations.<sup>18</sup>

This work is the first to consider low-dimensional-networked Br-based anti-perovskites. A comparison between the different halide sets reveals the generally greater Li-ion diffusion for the Br-containing systems, with  $\text{Li}_6\text{OBr}_4$  showing a very high self-diffusion coefficient of  $6.08 \times 10^{-9} \text{ cm}^2 \text{ s}^{-1}$  that is almost three times the value found for  $\text{Li}_6\text{OCl}_4$  ( $2.06 \times 10^{-9} \text{ cm}^2 \text{ s}^{-1}$ ). The prevalence of increased Li-ion diffusion in Br-containing systems is also seen for the 2DN and 1DN systems, with  $\text{Li}_4\text{OBr}_2$  and  $\text{Li}_5\text{OBr}_3$  showing self-diffusion coefficients of  $3.49 \times 10^{-10}$  and  $4.81 \times 10^{-9} \text{ cm}^2 \text{ s}^{-1}$ , respectively, compared to values of  $7.07 \times 10^{-11}$  and  $9.85 \times 10^{-10} \text{ cm}^2 \text{ s}^{-1}$  for  $\text{Li}_4\text{OCl}_2$  and  $\text{Li}_5\text{OCl}_3$ , respectively. The results in Fig. 7 show that the activation energies for the 3DN and 2DN systems are very similar for both sets of materials, ranging from 0.29 to 0.35 eV. Similar activation energies were also calculated for the 1DN and 0DN systems for both sets, with values ranging from 0.08 to 0.12 eV.

The only exception to the trend of increasing Li-ion diffusion with decreasing dimensionality is for  $\text{Li}_4\text{OCl}_2$ , which exhibits a self-diffusion coefficient at 300 K of  $7.07 \times 10^{-11} \text{ cm}^2 \text{ s}^{-1}$  and an activation energy of 0.33 eV, values that are lower and higher than the respective values for its 3DN counterpart,  $\text{Li}_3\text{OCl}$  ( $2.68 \times 10^{-10} \text{ cm}^2 \text{ s}^{-1}$  and 0.32 eV, respectively). This behaviour is perhaps expected given that the structure of  $\text{Li}_4\text{OCl}_2$  contains LiCl layers that represent barriers for Li-ion hopping, thereby resulting in 2D Li-ion diffusion. This is clearly illustrated by the Li-ion diffusion density plots presented in Fig. 8 for the Cl-based materials at 300 K (the equivalent plots for the Br-based materials are given in Fig. S3, ESI†). As illustrated, while strong isotropic 3D Li-ion diffusion is observed in  $\text{Li}_3\text{OCl}$ ,

$\text{Li}_5\text{OCl}_3$  and  $\text{Li}_6\text{OCl}_4$ , Li-ion diffusion in  $\text{Li}_4\text{OCl}_2$  is primarily restricted to the perovskite layer.

In contrast, as noted above, 2DN  $\text{Li}_4\text{OBr}_2$  does not exhibit the same reduction in Li-ion diffusion and increase in activation energy as 2DN  $\text{Li}_4\text{OCl}_2$  despite having the same structure. As shown by Fig. 8 and Fig. S3 (ESI†), this discrepancy is not related to the LiX (X = Cl or Br) layer as both materials primarily exhibit 2D Li-ion diffusion and the fact that the width of the LiBr layer is larger than that of the LiCl layer. This therefore suggests another fundamental reason why the 2D, 1D and 0D Br-based materials exhibit higher Li-ion diffusion than their Cl-based counterparts, as visualised in Fig. 8 and Fig. S3 (ESI†). An obvious explanation could be the increased volume of the Br-based materials; however, it has been shown that the bottlenecks for Li-ion transport in Br-based anti-perovskites are smaller than in Cl-based anti-perovskites, thereby potentially limiting it.<sup>52</sup>

Another factor to consider is the polarisability of the halide sublattice. It is well known that highly polarisable anion sublattices can have a significant effect on Li-ion conductivity in solid electrolytes by weakening the interaction between the Li ions and surrounding anions.<sup>75</sup> Several studies have shown that replacing the harder Cl ions with softer and more polarisable Br ions can result in significantly enhanced Li-ion transport.<sup>75–77</sup> Furthermore, the importance of a soft anion sublattice for fast Li-ion transport in hydride-based anti-perovskites has been revealed.<sup>20</sup> Given the inherent metastability/instability of the low-dimensional-networked materials in this study, it is likely that the presence of Br further weakens the Li-halide interactions, resulting in superionic Li-ion diffusion. This also raises the question of whether iodine doping in these systems could further enhance their ionic conductivity.

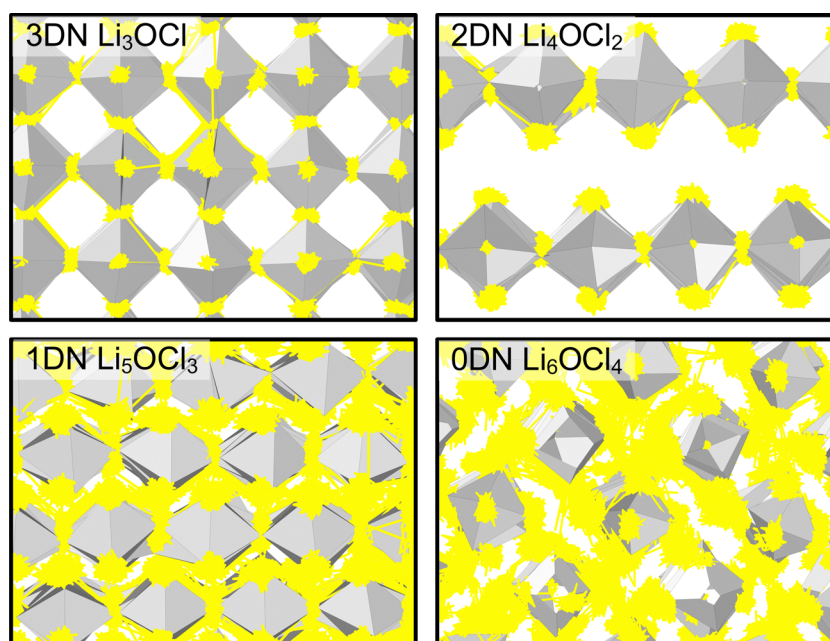


Fig. 8 Diffusion density plots of Li ions (yellow) overlaid on  $\text{OLi}_6$  (grey) octahedra in  $\text{Li}_x\text{OCl}_{x-2}$  ( $x = 3-6$ ) anti-perovskites at 300 K. Cl ions have been omitted for clarity.



As proposed previously for thiophosphate solid electrolytes, tailoring of the halide composition could also be an important strategy for tuning the conductivity and stability of anti-perovskite solid electrolytes.

We also assessed the impact of fluorine doping on Li-ion transport in the  $\text{Li}_x\text{OX}_{x-2}$  ( $X = \text{Cl}$  or  $\text{Br}$ ;  $x = 3-6$ ) systems. We considered doping at both the halide and oxygen (with Li vacancy charge compensation) sites at concentrations of 2% and 10%. Fig. 9 shows the Arrhenius dependencies for Li-ion diffusion in these anti-perovskite systems for F doping at the more energetically favourable halide sites with concentration of 2%.

Compared to the results for the undoped systems in Fig. 5, F doping causes a significant reduction in Li-ion conductivity for the majority of the systems and temperatures. Furthermore, substantial increases in the activation energy are observed as a result of F doping. These findings strongly suggest that the F

doping of these materials has a negative influence on their Li-ion transport performance. As discussed above, this further illustrates the important role of polarisability of the halide sublattice in anti-perovskite Li-ion conductors. The replacement of softer and more polarisable Cl and Br ions with F, as the least polarisable anion, is likely to strengthen the interaction between the Li ions and surrounding anions, resulting in reduced Li-ion conductivity.<sup>75</sup> Even larger activation energies were found for fluorine doping at the oxygen sites, as shown in Fig. S4 (ESI<sup>†</sup>). This is because in addition to the polarisability effect, in this case, the binding between the fluorine dopants and Li vacancies also inhibits long-range Li-ion diffusion, as predicted from the defect calculations above.<sup>28</sup> Fig. S4 (ESI<sup>†</sup>) shows that upon increasing the F doping concentration from 2% to 10%, there is generally a concomitant increase in the calculated activation energies. This further confirms the determinantal impact of F doping in these systems.

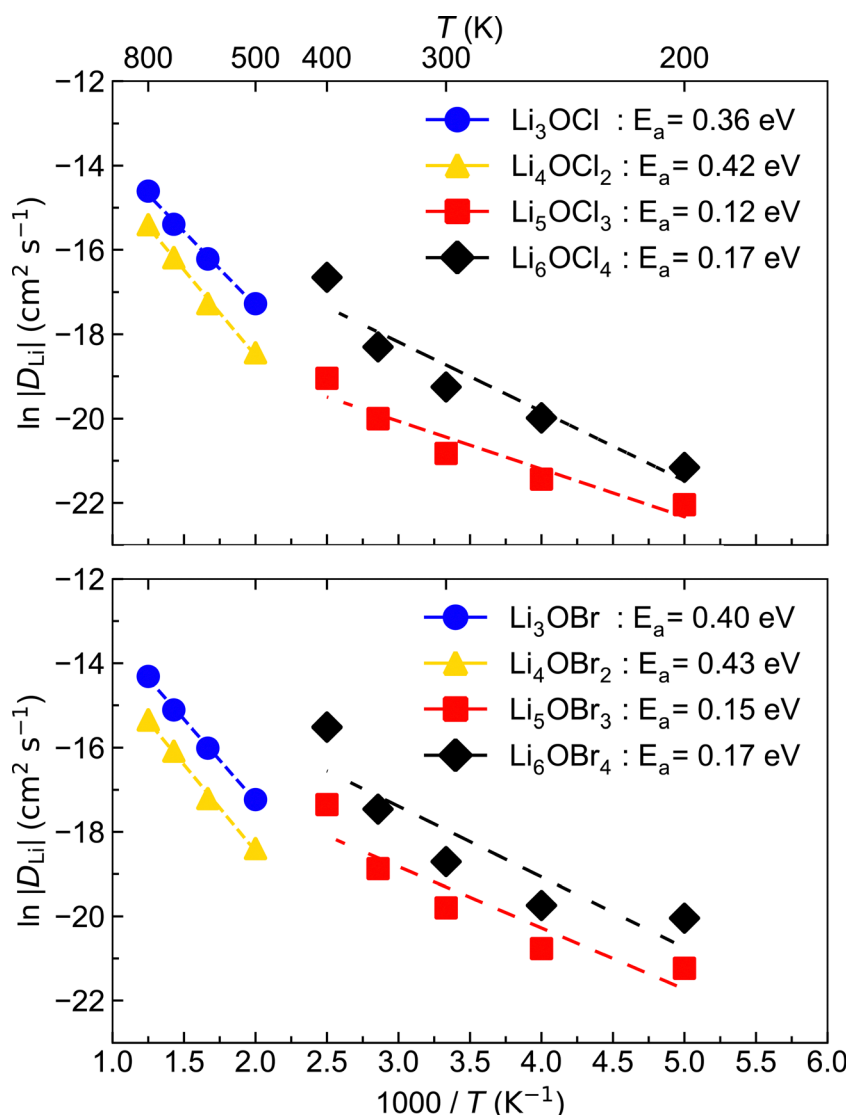


Fig. 9 Arrhenius plots of Li-ion diffusion for 2% F doping at the halide sites of  $\text{Li}_x\text{OX}_{x-2}$  ( $X = \text{Cl}$  (left) or  $\text{Br}$  (right);  $x = 3-6$ ) anti-perovskites.



## 4. Conclusion

In this work, we have explored the energetics of Schottky, Frenkel and antisite defect formation, stability and Li-ion transport in a wide range of undoped and F-doped  $\text{Li}_x\text{OX}_{x-2}$  ( $X = \text{Cl}$  or  $\text{Br}$ ;  $x = 3-6$ ) anti-perovskites with 3DN to 0DN structures. We find that defect formation for all systems becomes energetically more favourable as the dimensionality of the system is lowered. Additionally, we predict that the formation of the majority of defect types is more energetically favourable in Cl-containing systems rather than in systems with Br. With the exception of  $\text{Li}_6\text{OCl}_4$ , where Cl interstitials are the dominant type of intrinsic disorder, our results show that all the investigated systems are predicted to present Li-halide Schottky defect pairs as the dominant native defects. Fluorine doping at the halide sites is shown to be more energetically favourable than at the oxygen sites in these systems.

Using MD calculations and structural analysis, we predict the low-temperature melting of the 1DN and 0DN systems at temperatures as low as 300 K, highlighting the clear instability of these systems but potential for superionic Li-ion transport if they can be stabilised. We show that the Li-ion diffusion increases and the activation energy decreases with reducing dimensionality in these anti-perovskite materials. Furthermore, the highest Li-ion diffusion is found for the low-dimensional-networked Br-based materials, indicating that lattice polarisability plays an important role in these soft and unstable materials. The introduction of fluorine is found to be detrimental to Li-ion transport in these anti-perovskites as a result of its poor polarisability compared to Cl and Br and its binding to Li vacancies when doped at the oxygen sites.

Considering the critical importance of solid electrolytes in the development of solid-state batteries and the unique potential of anti-perovskite solid electrolytes, the results presented here can potentially guide future experimental synthesis choices and further advances in energy storage. Nevertheless, the preparation of these materials will have to account for their instability (or metastability), potentially through doping. Alternative synthesis routes may also provide a route their preparation, for example, mechanochemistry. Given the recent advances in the preparation and stabilisation of solid electrolytes, we are hopeful that variations of these materials will be reported in the near future.

## Conflicts of interest

There are no conflicts to declare.

## Acknowledgements

A. C. C. D. and J. A. D. thank the Newcastle University Academic Track (NUAcT) Fellowship Scheme for financial support. J. A. D. gratefully acknowledges the Engineering and Physical Sciences Research Council (EPSRC, EP/V013130/1) for funding. G. E. R. acknowledges support from the EPSRC CDT in Renewable Energy Northeast Universities (ReNU) for funding (EP/S023836/1).

Via membership of the UK's HEC Materials Chemistry Consortium, which is funded by the EPSRC (EP/R029431), this work used the ARCHER2 UK National Supercomputing Service. The Rocket High Performance Computing service at Newcastle University was also used.

## References

- 1 E. C. Evarts, Lithium batteries: to the limits of lithium, *Nature*, 2015, **526**, S93–S95.
- 2 K. Turcheniuk, D. Bondarev, V. Singhal and G. Yushin, Ten years left to redesign lithium-ion batteries, *Nature*, 2018, **559**, 467–470.
- 3 A. Masias, J. Marcicki and W. A. Paxton, Opportunities and Challenges of Lithium Ion Batteries in Automotive Applications, *ACS Energy Lett.*, 2021, **6**, 621–630.
- 4 N. Nitta, F. Wu, J. T. Lee and G. Yushin, Li-ion battery materials: present and future, *Mater. Today*, 2015, **18**, 252–264.
- 5 T. Famprikis, P. Canepa, J. A. Dawson, M. S. Islam and C. Masquelier, Fundamentals of inorganic solid-state electrolytes for batteries, *Nat. Mater.*, 2019, **18**, 1278–1291.
- 6 C. Li, Z. Yu Wang, Z. Jiang He, Y. Jiao Li, J. Mao, K. Hua Dai, C. Yan and J. Chao Zheng, An advance review of solid-state battery: challenges, progress and prospects, *Sustainable Mater. Technol.*, 2021, **29**, e00297.
- 7 J. A. Lewis, J. Tippens, F. J. Q. Cortes and M. T. McDowell, Chemo-Mechanical Challenges in Solid-State Batteries, *Trends Chem.*, 2019, **1**, 845–857.
- 8 J. Janek and W. G. Zeier, A solid future for battery development, *Nat. Energy*, 2016, **1**, 1–4.
- 9 Q. Zhao, S. Stalin, C. Z. Zhao and L. A. Archer, Designing solid-state electrolytes for safe, energy-dense batteries, *Nat. Rev. Mater.*, 2020, **5**, 229–252.
- 10 M. Pasta, D. Armstrong, Z. L. Brown, J. Bu, M. R. Castell, P. Chen, A. Cocks, S. A. Corr, E. J. Cussen, E. Darnbrough, V. Deshpande, C. Doerrer, M. S. Dyer, H. El-Shinawi, N. Fleck, P. Grant, G. L. Gregory, C. Grovenor, L. J. Hardwick, J. T. S. Irvine, H. J. Lee, G. Li, E. Liberti, I. McClelland, C. Monroe, P. D. Nellist, P. R. Shearing, E. Shoko, W. Song, D. S. Jolly, C. I. Thomas, S. J. Turrell, M. Vestli, C. K. Williams, Y. Zhou and P. G. Bruce, roadmap on solid-state batteries, *J. Phys. Energy*, 2020, **2**, 032008.
- 11 K. Kerman, A. Luntz, V. Viswanathan, Y.-M. Chiang and Z. Chen, Review—Practical Challenges Hindering the Development of Solid State Li Ion Batteries, *J. Electrochem. Soc.*, 2017, **164**, A1731–A1744.
- 12 S. Xia, X. Wu, Z. Zhang, Y. Cui and W. Liu, Practical Challenges and Future Perspectives of All-Solid-State Lithium-Metal Batteries, *Chem*, 2019, **5**, 753–785.
- 13 Y. Zhao and L. L. Daemen, Superionic conductivity in lithium-rich anti-perovskites, *J. Am. Chem. Soc.*, 2012, **134**, 15042–15047.
- 14 X. Lü, J. W. Howard, A. Chen, J. Zhu, S. Li, G. Wu, P. Dowden, H. Xu, Y. Zhao and Q. Jia, Antiperovskite  $\text{Li}_3\text{OCl}$



- superionic conductor films for solid-state Li-ion batteries, *Adv. Sci.*, 2016, **3**, 1500359.
- 15 H. Fang and P. Jena, Li-rich antiperovskite superionic conductors based on cluster ions, *Proc. Natl. Acad. Sci. U. S. A.*, 2017, **114**, 11046–11051.
  - 16 J. A. S. Serejo, J. S. Pereira, R. Mouta and L. G. C. Rego, Sluggish anion transport provides good kinetic stability to the anhydrous anti-perovskite solid electrolyte  $\text{Li}_3\text{OCl}$ , *Phys. Chem. Chem. Phys.*, 2021, **23**, 6964–6973.
  - 17 J. A. Dawson, T. Famprikis and K. E. Johnston, Antiperovskites for solid-state batteries: recent developments, current challenges and future prospects, *J. Mater. Chem. A*, 2021, **9**, 18746–18772.
  - 18 J. A. Dawson, P. Canepa, T. Famprikis, C. Masquelier and M. S. Islam, Atomic-Scale Influence of Grain Boundaries on Li-Ion Conduction in Solid Electrolytes for All-Solid-State Batteries, *J. Am. Chem. Soc.*, 2018, **140**, 362–368.
  - 19 Y. Li, W. Zhou, S. Xin, S. Li, J. Zhu, L. Xujie, Z. Cui, Q. Jia, J. Zhou, Y. Zhao and J. B. Goodenough, Fluorine-Doped Antiperovskite Electrolyte for All-Solid-State Lithium-Ion Batteries, *Angew. Chem., Int. Ed.*, 2016, **55**, 9965–9968.
  - 20 S. Gao, T. Broux, S. Fujii, C. Tassel, K. Yamamoto, Y. Xiao, I. Oikawa, H. Takamura, H. Ubukata, Y. Watanabe, K. Fujii, M. Yashima, A. Kuwabara, Y. Uchimoto and H. Kageyama, Hydride-based antiperovskites with soft anionic sublattices as fast alkali ionic conductors, *Nat. Commun.*, 2021, **12**, 1–10.
  - 21 K. Kim and D. J. Siegel, Correlating lattice distortions, ion migration barriers, and stability in solid electrolytes, *J. Mater. Chem. A*, 2019, **7**, 3216–3227.
  - 22 Z. Deng, B. Radhakrishnan and S. P. Ong, Rational composition optimization of the lithium-rich  $\text{Li}_3\text{OCl}_{1-x}\text{Br}_x$  antiperovskite superionic conductors, *Chem. Mater.*, 2015, **27**, 3749–3755.
  - 23 J. A. Dawson, H. Chen and M. Saiful Islam, Composition Screening of Lithium- and Sodium-Rich Anti-Perovskites for Fast-Conducting Solid Electrolytes, *J. Phys. Chem. C*, 2018, **122**, 23978–23984.
  - 24 A. Y. Song, Y. Xiao, K. Turcheniuk, P. Upadhyay, A. Ramanujapuram, J. Benson, A. Magasinski, M. Olguin, L. Meda, O. Borodin and G. Yushin, Protons Enhance Conductivities in Lithium Halide Hydroxide/Lithium Oxide Solid Electrolytes by Forming Rotating Hydroxy Groups, *Adv. Energy Mater.*, 2018, **8**, 1700971.
  - 25 J. A. Dawson, T. S. Attari, H. Chen, S. P. Emge, K. E. Johnston and M. S. Islam, Elucidating lithium-ion and proton dynamics in anti-perovskite solid electrolytes, *Energy Environ. Sci.*, 2018, **11**, 2993–3002.
  - 26 X. Lü, G. Wu, J. W. Howard, A. Chen, Y. Zhao, L. L. Daemen and Q. Jia, Li-rich anti-perovskite  $\text{Li}_3\text{OCl}$  films with enhanced ionic conductivity, *Chem. Commun.*, 2014, **50**, 11520–11522.
  - 27 S. Li, J. Zhu, Y. Wang, J. W. Howard, X. Lü, Y. Li, R. S. Kumar, L. Wang, L. L. Daemen and Y. Zhao, Reaction mechanism studies towards effective fabrication of lithium-rich anti-perovskites  $\text{Li}_3\text{OX}$  ( $X = \text{Cl}, \text{Br}$ ), *Solid State Ionics*, 2015, **284**, 14–19.
  - 28 M. J. Clarke, J. A. Dawson, T. J. Mays and M. S. Islam, Atomistic insights into the effects of doping and vacancy clustering on Li-ion conduction in the  $\text{Li}_3\text{OCl}$  antiperovskite solid electrolyte, *ACS Appl. Energy Mater.*, 2021, **4**, 5094–5100.
  - 29 E. Ahiavi, J. A. Dawson, U. Kudu, M. Courty, M. S. Islam, O. Clemens, C. Masquelier and T. Famprikis, Mechanochemical synthesis and ion transport properties of  $\text{Na}_3\text{OX}$  ( $X = \text{Cl}, \text{Br}, \text{I}$  and  $\text{BH}_4$ ) antiperovskite solid electrolytes, *J. Power Sources*, 2020, **471**, 228489.
  - 30 Z. Lu, C. Chen, Z. M. Baiyee, X. Chen, C. Niu and F. Ciucci, Defect chemistry and lithium transport in  $\text{Li}_3\text{OCl}$  antiperovskite superionic conductors, *Phys. Chem. Chem. Phys.*, 2015, **17**, 32547–32555.
  - 31 A. S. Bhalla, R. Guo and R. Roy, The perovskite structure—a review of its role in ceramic science and technology, *Mater. Res. Innov.*, 2000, **4**, 3–26.
  - 32 I. Hanghofer, G. J. Redhammer, S. Rohde, I. Hanzu, A. Senyshyn, H. M. R. Wilkening and D. Rettenwander, Untangling the Structure and Dynamics of Lithium-Rich Anti-Perovskites Envisaged as Solid Electrolytes for Batteries, *Chem. Mater.*, 2018, **30**, 8134–8144.
  - 33 A. Koedtrud, M. A. Patino, N. Ichikawa, D. Kan and Y. Shimakawa, Crystal structures and ionic conductivity in  $\text{Li}_2\text{OHX}$  ( $X = \text{Cl}, \text{Br}$ ) antiperovskites, *J. Solid State Chem.*, 2020, **286**, 121263.
  - 34 A. Y. Song, K. Turcheniuk, J. Leisen, Y. Xiao, L. Meda, O. Borodin and G. Yushin, Understanding Li-Ion Dynamics in Lithium Hydroxychloride ( $\text{Li}_2\text{OHCl}$ ) Solid State Electrolyte via Addressing the Role of Protons, *Adv. Energy Mater.*, 2020, **10**, 1903480.
  - 35 K. Shen, Y. Wang, J. Zhang, Y. Zong, G. Li, C. Zhao and H. Chen, Revealing the effect of grain boundary segregation on Li ion transport in polycrystalline anti-perovskite  $\text{Li}_3\text{ClO}$ : a phase field study, *Phys. Chem. Chem. Phys.*, 2020, **22**, 3030–3036.
  - 36 M. Wu, B. Xu, W. Luo, B. Sun, J. Shi and C. Ouyang, First-principles study on the structural, electronic, and Li-ion mobility properties of anti-perovskite superionic conductor  $\text{Li}_3\text{OCl}$  (1 0 0) surface, *Appl. Surf. Sci.*, 2020, **510**, 145394.
  - 37 H. J. Lee, B. Darminto, S. Narayanan, M. Diaz-Lopez, A. W. Xiao, Y. Chart, J. H. Lee, J. A. Dawson and M. Pasta, Li-ion conductivity in  $\text{Li}_2\text{OHCl}_{1-x}\text{Br}_x$  solid electrolytes: grains, grain boundaries and interfaces, *J. Mater. Chem. A*, 2022, **10**, 11574–11586.
  - 38 J. A. Dias, S. H. Santagneli and Y. Messaddeq, Methods for Lithium Ion NASICON Preparation: From Solid-State Synthesis to Highly Conductive Glass-Ceramics, *J. Phys. Chem. C*, 2020, **124**, 26518–26539.
  - 39 H. Fang, S. Wang, J. Liu, Q. Sun and P. Jena, Superhalogen-based lithium superionic conductors, *J. Mater. Chem. A*, 2017, **5**, 13373–13381.
  - 40 Y. Wang, Q. Wang, Z. Liu, Z. Zhou, S. Li, J. Zhu, R. Zou, Y. Wang, J. Lin and Y. Zhao, Structural manipulation approaches towards enhanced sodium ionic conductivity in Na-rich antiperovskites, *J. Power Sources*, 2015, **293**, 735–740.



- 41 J. Zhu, Y. Wang, S. Li, J. W. Howard, J. Neufeind, Y. Ren, H. Wang, C. Liang, W. Yang, R. Zou, C. Jin and Y. Zhao, Sodium Ion Transport Mechanisms in Antiperovskite Electrolytes  $\text{Na}_3\text{OBr}$  and  $\text{Na}_4\text{OI}_2$ : An in Situ Neutron Diffraction Study, *Inorg. Chem.*, 2016, **55**, 5993–5998.
- 42 H. Nguyen, S. Hy, E. Wu, Z. Deng, M. Samiee, T. Yersak, J. Luo, S. Ping Ong and Y. Shirley Meng, Experimental and Computational Evaluation of a Sodium-Rich Anti-Perovskite for Solid State Electrolytes, *J. Electrochem. Soc.*, 2016, **163**, 2165–2171.
- 43 A. Emly, E. Kioupakis and A. Van Der Ven, Phase stability and transport mechanisms in antiperovskite  $\text{Li}_3\text{OCl}$  and  $\text{Li}_3\text{OBr}$  superionic conductors, *Chem. Mater.*, 2013, **25**, 4663–4670.
- 44 R. Mouta, M. Á. B. Melo, E. M. Diniz and C. W. A. Paschoal, Concentration of charge carriers, migration, and stability in  $\text{Li}_3\text{OCl}$  solid electrolytes, *Chem. Mater.*, 2014, **26**, 7137–7144.
- 45 J. Howard, Z. D. Hood and N. A. W. Holzwarth, Fundamental aspects of the structural and electrolyte properties of  $\text{Li}_2\text{OHCl}$  from simulations and experiment, *Phys. Rev. Mater.*, 2017, **1**, 075406.
- 46 Z. Wang, H. Xu, M. Xuan and G. Shao, From anti-perovskite to double anti-perovskite: tuning lattice chemistry to achieve super-fast  $\text{Li}^+$  transport in cubic solid lithium halogen-chalcogenides, *J. Mater. Chem. A*, 2017, **6**, 73–83.
- 47 T. H. Wan, Z. Lu and F. Ciucci, A first principle study of the phase stability, ion transport and substitution strategy for highly ionic conductive sodium antiperovskite as solid electrolyte for sodium ion batteries, *J. Power Sources*, 2018, **390**, 61–70.
- 48 Y. Zhang, Y. Zhao and C. Chen, Ab initio study of the stabilities of and mechanism of superionic transport in lithium-rich antiperovskites, *Phys. Rev. B: Condens. Matter Mater. Phys.*, 2013, **87**, 134303.
- 49 S. Stegmaier, J. Voss, K. Reuter and A. C. Luntz,  $\text{Li}^+$  Defects in a Solid-State Li Ion Battery: Theoretical Insights with a  $\text{Li}_3\text{OCl}$  Electrolyte, *Chem. Mater.*, 2017, **29**, 4330–4340.
- 50 M. H. Chen, A. Emly and A. Van Der Ven, Anharmonicity and phase stability of antiperovskite  $\text{Li}_3\text{OCl}$ , *Phys. Rev. B: Condens. Matter Mater. Phys.*, 2015, **91**, 214306.
- 51 R. Mouta, E. M. Diniz and C. W. A. Paschoal,  $\text{Li}^+$  interstitials as the charge carriers in superionic lithium-rich antiperovskites, *J. Mater. Chem. A*, 2016, **4**, 1586–1590.
- 52 S. Zhao, C. Chen, H. Li and W. Zhang, Theoretical insights into the diffusion mechanism of alkali ions in Ruddlesden-Popper antiperovskites, *New J. Chem.*, 2021, **45**, 4219–4226.
- 53 J. G. Smith and D. J. Siegel, Low-temperature paddlewheel effect in glassy solid electrolytes, *Nat. Commun.*, 2020, **11**, 1–11.
- 54 X. He, Y. Zhu and Y. Mo, Origin of fast ion diffusion in super-ionic conductors, *Nat. Commun.*, 2017, **8**, 1–7.
- 55 R. Jalem, Y. Yamamoto, H. Shiiba, M. Nakayama, H. Munakata, T. Kasuga and K. Kanamura, Concerted migration mechanism in the Li ion dynamics of garnet-type  $\text{Li}_7\text{La}_3\text{Zr}_2\text{O}_{12}$ , *Chem. Mater.*, 2013, **25**, 425–430.
- 56 A. M. Nolan, Y. Zhu, X. He, Q. Bai and Y. Mo, Computation-Accelerated Design of Materials and Interfaces for All-Solid-State Lithium-Ion Batteries, *Joule*, 2018, **2**, 2016–2046.
- 57 Z. Lu, J. Liu and F. Ciucci, Superionic conduction in low-dimensional-networked anti-perovskites, *Energy Storage Mater.*, 2020, **28**, 146–152.
- 58 M. I. Saidaminov, O. F. Mohammed and O. M. Bakr, Low-Dimensional-Networked Metal Halide Perovskites: The Next Big Thing, *ACS Energy Lett.*, 2017, **2**, 889–896.
- 59 J. Zhu, S. Li, Y. Zhang, J. W. Howard, X. Lü, Y. Li, Y. Wang, R. S. Kumar, L. Wang and Y. Zhao, Enhanced ionic conductivity with  $\text{Li}_7\text{O}_2\text{Br}_3$  phase in  $\text{Li}_3\text{OBr}$  anti-perovskite solid electrolyte, *Appl. Phys. Lett.*, 2016, **109**, 101904.
- 60 S. Wakazaki, Q. Liu, R. Jalem, T. Nishikubo, Y. Sakai, N. Matsui, G. Zhao, K. Suzuki, K. Shigematsu, T. Yamamoto, R. Kanno, H. Das, Y. Tateyama and M. Azuma, High-Pressure Synthesis and Lithium-Ion Conduction of  $\text{Li}_4\text{OBr}_2$  Derivatives with a Layered Inverse-Perovskite Structure, *Chem. Mater.*, 2021, **33**, 9194–9201.
- 61 H. Sabrowsky, K. Paszkowski, D. Reddig and P. Vogt,  $\text{Na}_3\text{OCl}$  und  $\text{Na}_3\text{OBr}$ , die ersten Alkalimetallchalcogenidhalogenide  $\text{Na}_3\text{OCl}$  und  $\text{Na}_3\text{OBr}$ , the First Alkali Metal Chalcogenide Halides, *Z. Naturforsch.*, 1988, **43**, 238–239.
- 62 M. S. Islam and C. A. J. Fisher, Lithium and sodium battery cathode materials: computational insights into voltage, diffusion and nanostructural properties, *Chem. Soc. Rev.*, 2014, **43**, 185–204.
- 63 F. N. Forrester, J. A. Quirk, T. Famprakis and J. A. Dawson, Disentangling Cation and Anion Dynamics in  $\text{Li}_3\text{PS}_4$  Solid Electrolytes, *Chem. Mater.*, 2022, **34**, 10561–10571.
- 64 S. M. Wood, C. Eames, E. Kendrick and M. S. Islam, Sodium Ion Diffusion and Voltage Trends in Phosphates  $\text{Na}_4\text{M}_3(\text{PO}_4)_2\text{P}_2\text{O}_7$  ( $\text{M} = \text{Fe}, \text{Mn}, \text{Co}, \text{Ni}$ ) for Possible High-Rate Cathodes, *J. Phys. Chem. C*, 2015, **119**, 15935–15941.
- 65 J. C. Treacher, S. M. Wood, M. S. Islam and E. Kendrick,  $\text{Na}_2\text{CoSiO}_4$  as a cathode material for sodium-ion batteries: structure, electrochemistry and diffusion pathways, *Phys. Chem. Chem. Phys.*, 2016, **18**, 32744–32752.
- 66 Y. Deng, C. Eames, B. Fleutot, R. David, J. N. Chotard, E. Suard, C. Masquelier and M. S. Islam, Enhancing the Lithium Ion Conductivity in Lithium Superionic Conductor (LISICON) Solid Electrolytes through a Mixed Polyanion Effect, *ACS Appl. Mater. Interfaces*, 2017, **9**, 7050–7058.
- 67 A. D. Poletayev, J. A. Dawson, M. S. Islam and A. M. Lindenberg, Defect-driven anomalous transport in fast-ion conducting solid electrolytes, *Nat. Mater.*, 2022, **21**, 1066–1073.
- 68 A. Jain, S. P. Ong, G. Hautier, W. Chen, W. D. Richards, S. Dacek, S. Cholia, D. Gunter, D. Skinner, G. Ceder and K. A. Persson, Commentary: The Materials Project: a materials genome approach to accelerating materials innovation, *APL Mater.*, 2013, **1**, 011002.
- 69 B. G. Dick and A. W. Overhauser, Theory of the Dielectric Constants of Alkali Halide Crystals, *Phys. Rev.*, 1958, **112**, 90.
- 70 J. D. Gale and A. L. Rohl, *The General Utility Lattice Program (GULP)*, 2011, **29**, 291–341, DOI: [10.1080/089270203100104887](https://doi.org/10.1080/089270203100104887).
- 71 M. J. Mott and N. F. Littleton, Conduction in Polar Crystals. I. Electrolytic Conduction in Solid Salts, *Trans. Faraday Soc.*, 1938, **34**, 485–499.



- 72 S. Plimpton, Fast Parallel Algorithms for Short-Range Molecular Dynamics, *JCoPh*, 1995, **117**, 1–19.
- 73 D. J. Evans, B. L. Holian, D. J. Evans and B. L. Holian, The Nose–Hoover thermostat, *J. Chem. Phys.*, 1998, **83**, 4069.
- 74 A. G. Squires, J. M. Dean and B. J. Morgan, Aliovalent doping response and impact on ionic conductivity in the antiperovskite solid electrolyte  $\text{Li}_3\text{OCl}$ , *ChemRxiv*, 2021, **1**, 1–14.
- 75 M. A. Kraft, S. P. Culver, M. Calderon, F. Bo, T. Krauskopf, A. Senyshyn, C. Dietrich, A. Zevalkink, J. Janek and W. G. Zeier, Influence of Lattice Polarizability on the Ionic Conductivity in the Lithium Superionic Argyrodites  $\text{Li}_6\text{PS}_5\text{X}$  (X = Cl, Br, I), *J. Am. Chem. Soc.*, 2017, **139**, 10909–10918.
- 76 K. Kaup, A. Assoud, J. Liu and L. F. Nazar, Fast Li-Ion Conductivity in Superadamantanoid Lithium Thioborate Halides, *Angew. Chem., Int. Ed.*, 2021, **60**, 6975–6980.
- 77 I. Hanghofer, B. Gadermaier, H. Martin and R. Wilkening, Fast Rotational Dynamics in Argyrodite-Type  $\text{Li}_6\text{PS}_5\text{X}$  (X: Cl, Br, I) as Seen by  $^{31}\text{P}$  Nuclear Magnetic Relaxation-On Cation-Anion Coupled Transport in Thiophosphates, *Chem. Mater.*, 2019, **31**, 4591–4597.

